



International Committee for Future Accelerators

Sponsored by the Particles and Fields Commission of IUPAP

Beam Dynamics Newsletter

No. 45

**Issue Editor:
R. Wanzenberg**

**Editor in Chief:
W. Chou**

April 2008

4.2 Computation of Short Range Wake Fields with PBCI

Erion Gjonaj, Thomas Lau, Thomas Weiland
 TUD, TEMF, Schlossgartenstr. 8, 64283 Darmstadt, Germany
 Rainer Wanzenberg
 Deutsches Elektronen-Synchrotron, A Research Centre of Helmholtz Association
 Notkestr. 85, 22603 Hamburg, Germany
 Mail to: gjonaj@temf.de

4.2.1 Introduction

4.2.1.1 Wake Fields and Wake Field Instabilities

An ultra-relativistic electron beam passing through an accelerator cavity generates electromagnetic wake fields. Wake fields act back on the beam and, thus, influence its dynamics. The beam-cavity interaction via wake fields may lead to degradation of beam quality (emittance growth, energy spread) or even to collective instabilities [1-3]. Such instabilities pose the main limitation on the maximum achievable current per bunch or on the total beam current or on both of them.

The integral quantity which describes the total wake field force on an electron bunch traveling in the z -direction is the wake potential,

$$\bar{W}(s) = \frac{1}{Q} \int_{-\infty}^{+\infty} dz' (\bar{E} + c \bar{e}_z \times \bar{B})_{t=(z'+s)/c}, \quad (1)$$

where Q is the bunch charge, \bar{E} and \bar{B} are the electromagnetic fields evaluated at the retarded time with respect to the relative position s within the bunch [4]. The effect of wake fields on the beam dynamics can be roughly estimated from the analysis of the wake potential (1). Electromagnetic fields associated with short electron bunches are high frequency fields. They propagate within the cavity with nearly the speed of light in vacuum, almost synchronously with the bunch. The corresponding wake potential (1) is a short range function which is restricted to small values of s . Thus, the wake field of a short electron bunch represents, in the first place, a source for single-bunch instabilities. Contrary, the low frequency wake fields generated by long bunches tend to dwell in the cavity for a very long time. Such wakes are often referred to as captured modes. They are responsible for multi-bunch instabilities which arise from the interaction between consecutive bunches passing through the cavity.

Apart from the wake potential (1), other quantities of interest are the loss parameter, k_{\parallel} , and the kick parameter, k_{\perp} . These are defined as:

$$k_{\parallel} = \int_{-\infty}^{+\infty} ds \rho(s) \cdot W_{\parallel}(s), \quad k_{\perp} = \int_{-\infty}^{+\infty} ds \rho(s) \cdot W_{\perp}(s), \quad (2)$$

where W_{\parallel} and W_{\perp} are the longitudinal and transversal components of the wake potential (1), respectively, and ρ is the normalized bunch charge density. The loss parameter can be considered as a measure for the energy spread experienced by the bunch due to wake

field interaction. The kick factor is useful for the estimation of emittance growth within the cavity. Another parameter related to the beam-wake interaction is,

$$k_{\parallel}(1) = \int_{-\infty}^{+\infty} ds \rho(s) \cdot \frac{d}{ds} W_{\parallel}(s). \quad (3)$$

This parameter is often used in the calculation of the synchrotron tune shift for the longitudinally coupled mode instabilities in storage rings such as PETRA III [5, 6].

The present paper is concerned with the numerical calculation of the wake field related quantities (1)-(3) in the context of the X-FEL and the ILC projects. These projects require high luminosity beams with ultra-short electron bunches. The rms bunch length for the ILC is 150 μm [7]; for the X-FEL as low as 25 μm [8]. The main focus is, therefore, on the computation of short range wake fields. From the numerical point of view, wake field simulations are very challenging. This is mainly related to the large computational resources which are needed for an appropriate discretization of the extremely high-frequency fields (in the X-FEL case, with frequencies of up to 5THz [8]). Furthermore, fully 3D simulations are required in order to account for the often complex geometries of the accelerator structures involved.

4.2.1.2 Numerical Solutions in Wake Field Computation

In the course of the past 20 years, several wake field simulation codes have been used with considerable success in accelerator design. Table 1 gives a brief overview on the available wake field codes and their properties. There exists an extensive literature on each of these codes. Of particular importance, however, are the numerical algorithms which have been developed in the context of wake field simulations.

The *moving window* technique for ultra-relativistic bunches (Bane et al [9]) and the *indirect path* wake potential integration (Weiland [10], Napoly et al [11]) represent two important milestones in this development. In the moving window technique, discretization is applied only on a comparatively small computational grid which encloses the ultra-relativistic bunch while moving along the accelerator with the speed of light in vacuum. This approach allows for a very efficient calculation of short range wake fields. The indirect path wake potential integration allows for the computation of wake field contributions in outgoing beam pipes using a semi-analytical approach. The indirect integration technique was originally introduced for rotationally symmetric structures. Recently, a number of generalizations of this approach for arbitrary 3D geometries have been proposed [12, 13].

In a pioneering work of Zagorodnov et al [14], a novel 3D discretization technique for Maxwell equations with *no longitudinal dispersion* was introduced. This property of the numerical scheme is prerequisite for a moving window implementation, since in this case, the numerical phase velocity of longitudinal waves must exactly match the speed of light in vacuum. An important extension of this work was the Uniformly Stable Conformal (USC) scheme [15] for the Finite Integration Technique (FIT). This scheme allows for the application of a *boundary conformal* approximation in a moving window implementation.

Code *parallelization* is another key issue in wake field simulation. The huge computational resources required by the simulation of short electron bunches in 3D geometry can only be handled in a parallel computing environment. Hereby, as the

bunch lengths become shorter, the accurate but computationally expensive conformal approximation of geometrical boundaries appears to be of less importance for the overall simulation quality. In many cases, the spatial resolution required by the short wave lengths involved in the simulations is by far sufficient for an appropriate geometry approximation even when a simple stair-step geometry representation is used.

Recent developments have seen the implementation of high order Finite Element Methods (FEM) in wake field computations [16, 17]. These methods allow for highly accurate electromagnetic field solutions. At the current stage, however, the use of unstructured or boundary fitted grids associated with the application of these methods requires a static computational window. This is an important limitation on efficiency, since the computational costs associated with the spatial discretization increase linearly with the length of the cavity to be simulated.

Table 1: Attempted listing of the available wake field codes.

Code	Dispersionless	Moving Window	Conformal	Parallel
TBCI / URMEL	–	+	–	–
NOVO	+	–	–	–
MAFIA	–	+	–	–
ABCI	–	+	–	–
GDFIDL	–	–	+	+
ECHO	+	+	+	–
TAU3P	–	–	+	+
CST Particle Studio	–	–	+	–
PBCI	+	+	–	+
NEKCEM	–	–	+	+

In the following, the Parallel Beam Cavity Interaction (PBCI) code is discussed. PBCI is designed for massively parallel wake field simulations in arbitrary 3D geometry. The algorithms use a dispersionless split-operator scheme as well as a domain decomposition approach for balanced parallel computations. A description of these algorithms is given in Section 1.1.2. The rest of the paper is dedicated to a number of wake field applications in the context of the X-FEL and ILC projects.

4.2.2 The PBCI Code

4.2.2.1 Finite Integration Technique

The discretization of electromagnetic fields in PBCI is based on the Finite Integration Technique (FIT) [18]. The semi discrete equations of FIT are

$$\frac{d}{dt} \begin{pmatrix} \widehat{\mathbf{e}} \\ \widehat{\mathbf{h}} \end{pmatrix} = \begin{pmatrix} \mathbf{0} & \mathbf{M}_\varepsilon^{-1} \mathbf{C}^T \\ -\mathbf{M}_\mu^{-1} \mathbf{C} & \mathbf{0} \end{pmatrix} \begin{pmatrix} \widehat{\mathbf{e}} \\ \widehat{\mathbf{h}} \end{pmatrix} - \begin{pmatrix} \mathbf{M}_\varepsilon^{-1} \widehat{\mathbf{j}} \\ \mathbf{0} \end{pmatrix}, \quad (4)$$

where the unknowns, $\widehat{\mathbf{e}}$ and $\widehat{\mathbf{h}}$, are interpreted as electric and magnetic voltages along the edges of a dual-orthogonal pair of staggered grids and $\widehat{\mathbf{j}}$ is the excitation current.

The operator \mathbf{C} denotes the topological curl: \mathbf{M}_ε and \mathbf{M}_μ are the positive definite and diagonal material operators of FIT.

The integration of (4) in time is typically performed by applying an explicit time-marching scheme of the form

$$\begin{pmatrix} \widehat{\mathbf{e}} \\ \widehat{\mathbf{h}} \end{pmatrix}^{n+1} = \mathbf{G}(\Delta t) \begin{pmatrix} \widehat{\mathbf{e}} \\ \widehat{\mathbf{h}} \end{pmatrix}^n - \begin{pmatrix} \Delta t \mathbf{M}_\varepsilon^{-1} \widehat{\mathbf{j}} \\ \mathbf{0} \end{pmatrix}^n. \quad (5)$$

In (5), $\mathbf{G}(\Delta t)$ represents the specific evolution operator of the time integration scheme, and Δt is the integration time step. For the commonly used leapfrog integrator this operator is explicitly given by

$$\mathbf{G}(\Delta t) = \begin{pmatrix} \mathbf{1} & \Delta t \mathbf{M}_\varepsilon^{-1} \mathbf{C}^T \\ -\Delta t \mathbf{M}_\mu^{-1} \mathbf{C} & \mathbf{1} - \Delta t^2 \mathbf{M}_\mu^{-1} \mathbf{C} \mathbf{M}_\varepsilon^{-1} \mathbf{C}^T \end{pmatrix}. \quad (6)$$

The leapfrog-FIT scheme has been thoroughly investigated in terms of stability and dispersion properties. In particular, for Cartesian grids it can be shown that the dispersion error is largest for waves propagating in the direction of coordinate axes (see below). This property of the scheme is responsible for the large dispersion error (numerical noise) which is often observed in particle beam simulations. This is because the longitudinal waves associated with the bunch motion dominate the high-frequency electromagnetic field spectrum.

Yet another drawback of the leapfrog scheme is that no moving computational window can be used in wake field simulations with ultra-relativistic bunches. Since the longitudinal phase velocity of the numerical field solution does not exactly match the speed of light in vacuum, unphysical reflections are produced at the boundaries of the moving computational window. These errors increase systematically with simulation time, thus, deteriorating numerical accuracy.

4.2.2.2 Dispersionless Split-Operator Scheme

The idea of split-operator methods is based on the modification of the evolution operator $\mathbf{G}(\Delta t)$ such that no numerical dispersion occurs in the longitudinal, bunch propagation direction. The split-operator scheme used in PBCI was originally developed for the purpose of suppressing numerical noise in self-consistent Particle-In-Cell (PIC) simulations [19]. It is obtained by decomposing $\mathbf{G}(\Delta t)$ into longitudinal and transversal parts using the second order accurate, *Strang splitting* procedure [20]. The resulting Longitudinal-Transversal (LT) splitting scheme reads

$$\begin{pmatrix} \widehat{\mathbf{e}} \\ \widehat{\mathbf{h}} \end{pmatrix}^{n+1} = \mathbf{G}_t \left(\frac{\Delta t}{2} \right) \mathbf{G}_l(\Delta t) \mathbf{G}_t \left(\frac{\Delta t}{2} \right) \begin{pmatrix} \widehat{\mathbf{e}} \\ \widehat{\mathbf{h}} \end{pmatrix}^n - \begin{pmatrix} \Delta t \mathbf{M}_\varepsilon^{-1} \widehat{\mathbf{j}} \\ \mathbf{0} \end{pmatrix}^n. \quad (7)$$

The propagators, $\mathbf{G}_l(\Delta t)$ and $\mathbf{G}_t(\Delta t)$, contain only spatial derivatives in the longitudinal and transversal directions, respectively. Thus, the two transversal updates

in (7) will not affect plane wave solutions propagating in the longitudinal direction, whereas the longitudinal update, $\mathbf{G}_l(\Delta t)$, represents the time evolution of a simple one dimensional system.

The LT scheme is completed by replacing each of the time evolution operators in (7) with second order accurate *Verlet-leapfrog* propagators. In matrix operator form they can be written as

$$\mathbf{G}_{l;t}(\Delta t) = \begin{pmatrix} \mathbf{1} - \frac{\Delta t^2}{2} \mathbf{M}_\varepsilon^{-1} \mathbf{C}_{l;t}^T \mathbf{M}_\mu^{-1} \mathbf{C}_{l;t} & \Delta t \mathbf{M}_\varepsilon^{-1} \mathbf{C}_{l;t}^T - \frac{\Delta t^3}{4} \mathbf{M}_\varepsilon^{-1} \mathbf{C}_{l;t}^T \mathbf{M}_\mu^{-1} \mathbf{C}_{l;t} \mathbf{M}_\varepsilon^{-1} \mathbf{C}_{l;t}^T \\ -\Delta t \mathbf{M}_\mu^{-1} \mathbf{C}_{l;t} & \mathbf{1} - \frac{\Delta t^2}{2} \mathbf{M}_\mu^{-1} \mathbf{C}_{l;t} \mathbf{M}_\varepsilon^{-1} \mathbf{C}_{l;t}^T \end{pmatrix}. \quad (8)$$

Exact numerical dispersion relations for the LT scheme using von Neumann analysis have been derived in [19]. Here, we only show the behavior of the numerical phase velocity as compared to the standard leapfrog scheme. Figure 1 shows normalized numerical phase velocities in the xz -plane, which are computed from the dispersion relations as, $v = \omega/(ck)$, where ω and k are the numerical frequency and wave number, respectively, and c is the speed of light in vacuum. In each of the two graphs, two different grid resolutions have been used.

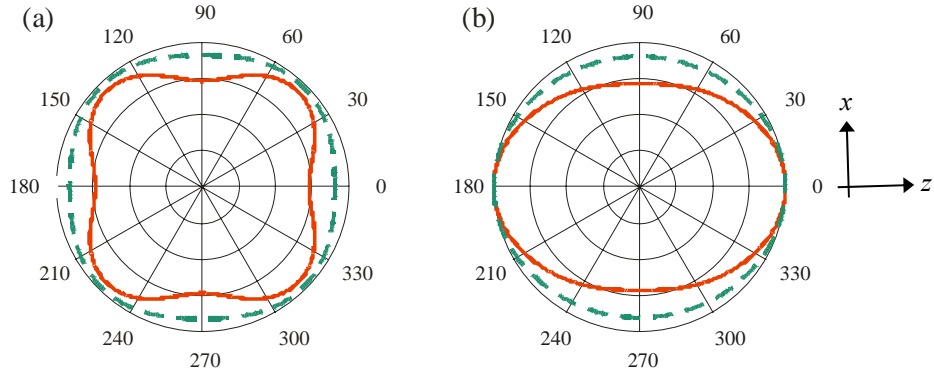


Figure 1: Normalized numerical phase velocities for the (a) leapfrog and (b) LT schemes in the xz -plane. The solid and dashed lines show the normalized phase velocities for a grid resolution of 5 and 10 grid points / wave length, respectively. In (b), the “magic time step” is used.

The dispersion error of the leapfrog scheme becomes largest in the directions of coordinate axes. Contrary, the LT scheme (Fig. 1b) minimizes the dispersion error in the longitudinal, z -direction. Thus, the effect of operator splitting consists in rotating the optimum dispersion direction in the longitudinal direction. In particular, at the so called “magic time step”, $\Delta t = \Delta z / c$, the LT scheme has no numerical dispersion along this direction (see Fig. 1b). The exact propagation of longitudinal waves allows for a moving window implementation. Additionally, the integration scheme (4) is purely explicit in time which makes the time stepping algorithm easily parallelizable.

4.2.2.3 Termination Conditions for Long Beam Pipes

Wake fields generated by a geometrical discontinuity on the accelerator walls may *catch-up* the bunch at a very large distance (time) behind the discontinuity. For any

fixed traveling distance, z , within the structure, a longitudinal wake potential can be defined as

$$W_z(s, z) = \frac{1}{Q} \int_{-\infty}^z dz' E_z \left(x, y, z', t = \frac{z' + s}{c} \right). \quad (9)$$

The total longitudinal wake potential is, then, $W_z(s, \infty)$. The numerical integration of $W_z(s, \infty)$ in the time domain, however, is often impossible. The distance where the bunch is caught by the wake fields is inversely proportional to the bunch length. Thus, in particular, for short electron bunches, the integration time becomes prohibitively large for a full time domain simulation.

The simple approach used in PBCI for overcoming this difficulty is schematically shown in Fig. 2. The total wake potential is separated into a “direct part”, $W_z(s, 0)$, containing the incoming beam pipe and the discontinuity, and a “transient part” which accounts for the wake field force in the outgoing pipe. The direct wake potential is integrated according to (9) using the time domain simulation data. For the computation of the transient wake potential a modal expansion of the electromagnetic field solution in a transversal plane within the outgoing pipe is performed. Assuming the location of the plane at $z = 0$, the general form of such an expansion is

$$E_z(x, y, 0, t) = \int_{-\infty}^{\infty} d\omega \sum_n c_n(\omega) e_z^n(x, y) \exp(i\omega t) \quad (10)$$

where $e_z^n(x, y)$, is the n -th (TM) eigenmode solution in the pipe and $c_n(\omega)$ is the frequency domain spectral coefficient of the mode extracted by Fourier analysis. Using (10) and the vanishing of wake fields at infinity, the wake potential contribution of a single wave guide mode within the pipe,

$$W_n(s) = \int_0^{\infty} dz' \int_{-\infty}^{\infty} d\omega c_n(\omega) \exp \left[ik_n(\omega)z' - i\omega \frac{z' + s}{c} \right], \quad (11)$$

is readily found to

$$W_n(s) = \int_{-\infty}^{\infty} d\omega \frac{c_n(\omega)}{i[\omega/c - k_n(\omega)]} \exp \left(-i\omega \frac{s}{c} \right), \quad (12)$$

where $k_n(\omega)$ is the wave number of the mode. The total longitudinal wake potential is, then, given by

$$W_z(s, \infty) = W_z(s, 0) + \frac{1}{Q} \sum_n e_z^n(x, y) W_n(s). \quad (13)$$

From the point of view of numerical implementation, the above procedure includes the solution of a 2D eigenmode problem in the outgoing pipe, the Fourier analysis of the modal coefficients and the inverse Fourier transforms (12). Hereby, the number of wave guide modes considered in the analysis may be critical to the validity of numerical

results. However, since only a 2D eigenmode problem needs to be solved, the calculation of a large number (several hundred) of modes can be typically performed with a comparably small computational effort.

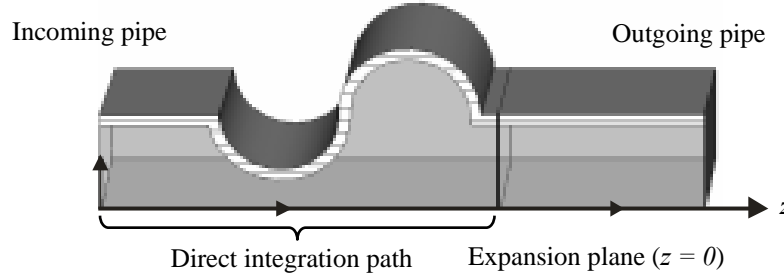


Figure 2: Separation of the wake potential computation into a direct part and a transient part in the outgoing beam pipe.

Apart from the explicit frequency domain representation of the modal coefficients, the procedure used in PBCI is equivalent to the approach proposed in [13, 21]. In [13], the inverse Fourier transform (12) is avoided by introducing centered differences in time and space for the time dependent modal coefficients. Maintaining the explicit frequency domain representation, however, is of advantage for purposes other than the calculation of wake potentials. In particular, this representation allows for the reconstruction of the full time domain simulation data at any downstream position in the outgoing pipe.

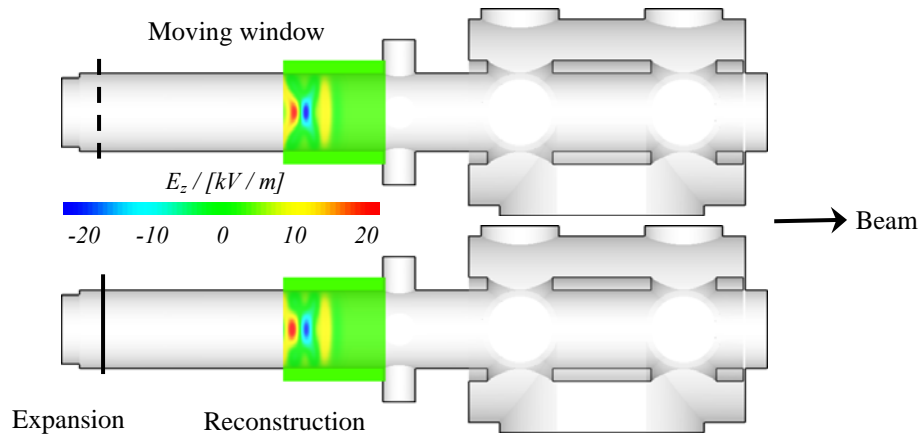


Figure 3: Time domain simulation (top) vs. frequency domain reconstruction within the moving window (bottom) in the separating pipe of PITZ. For illustration, only 15 waveguide modes were used in the reconstruction.

Such a situation is illustrated in Fig. 3. Exemplarily, the PITZ diagnostics section [22] (see also Section 4.2.3.2) is considered. About one third of the structure consists of a homogeneous pipe separating a small step at the entrance from the rest of the structure. The modal expansion is performed shortly behind the step. Using the frequency domain representation, the full electromagnetic field solution is reconstructed within the moving window at the end of the pipe. There, the time domain wake field simulation for the rest of the structure is resumed. This procedure results in considerable

computational savings when the cavity consists of a number of inhomogeneous sections separated by long beam pipes.

4.2.2.4 Code Parallelization

In 3D simulations involving short electron bunches, huge computational resources in terms of both memory and CPU time are needed. Such simulations can only be handled in a parallel computing environment (cluster). The parallelization model used in PBCI is based on a geometrical decomposition of the computational domain (partitioning) between the single processes in the cluster. Each processing node is responsible for performing computational tasks on the field data contained within the respective subdomain.

In Fig. 4, the partitioning approach is shown schematically for a three-node cluster. Starting with the global computational domain, an orthogonal bisection procedure is recursively applied. The procedure results in a binary tree, whose internal nodes are intermediate subdomains whereas the leaf nodes correspond to active (computational) subdomains. Because of the local nature of the FIT operators, only field values residing on the subdomain boundaries need to be exchanged in the computation. For Cartesian grids, the orthogonal bisection approach minimizes the number of such boundary values and, thus, the communication overhead in the field update equations.

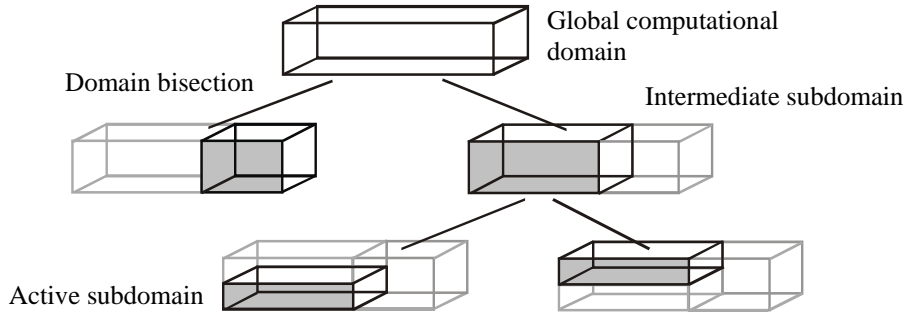


Figure 4: Example decomposition of the computational domain on a three-node cluster.

In order to determine the optimum partitioning which results in equally balanced workloads among the processing nodes, PBCI implements the load balancing scheme proposed in [23] for Particle-In-Cell simulations. The bisection procedure is performed on the basis of computational weights W_i which are assigned to each grid point. The total computational load associated with a given intermediate subdomain is, $W = \sum W_i$, where the summation includes only grid points within the subdomain. If the subdomain has to be partitioned between N processes, the bisection is such that

$$\frac{W_{\text{left}}}{W_{\text{right}}} = \frac{N_{\text{left}}}{N_{\text{right}}}, \quad \text{with} \quad N_{\text{left}} = \left\lceil \frac{N}{2} \right\rceil, \quad N_{\text{right}} = \left\lfloor \frac{N}{2} \right\rfloor \quad (14)$$

where W_{left} , W_{right} and N_{left} , N_{right} are the computational weights and the number of processes, respectively, assigned to the two subdomains created by subdivision. This algorithm allows for an almost ideally balanced distribution of computational

workloads. In addition, it can be applied to simulations involving an arbitrary number of processors on heterogeneous clusters.

4.2.3 Applications

4.2.3.1 Tapered Transition for PETRA III

PETRA III [6] will serve as a dedicated 3rd generation synchrotron radiation facility at DESY. The impedance model presented in [24, 29] shows that an important contribution to the total impedance budget of PETRA III comes from the tapered transitions which are installed between the “standard” vacuum chamber and the undulator vacuum chamber. A total of 16 such transitions will be used in the ring. The basic geometry of the tapered transition including the vacuum pumping ports is shown in Fig. 5. The detailed geometrical dimensions for two slightly different geometrical configurations (referred to as Variant 1 and 2) can be found in [25].

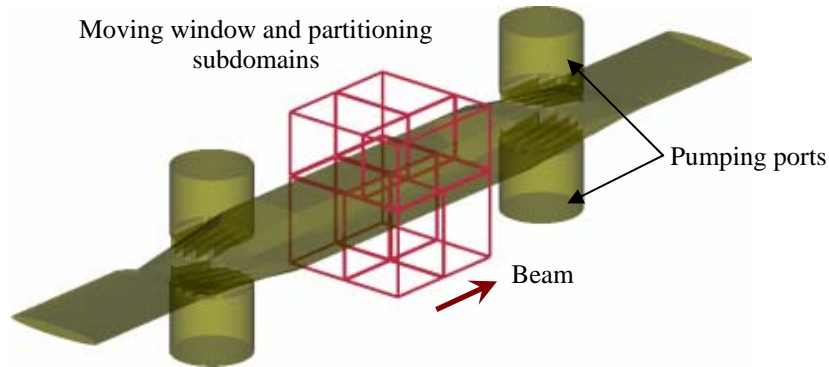


Figure 5: Geometry of the tapered transition together with a schematic view of the moving computational window. The subdomain bounds of the resulting parallel partitioning are shown as red lines for an exemplary computation on 7 processors.

The wake potentials of the tapered transition have been calculated with MAFIA [26] and PBCI for different mesh resolutions. Although the electron bunch considered in the simulations is comparably long ($\sigma = 10\text{mm}$), the geometrical complexity of the structure with a total length of $L \approx 1\text{m}$, necessarily leads to a large computational mesh. Figure 5 illustrates the moving window approach used in PBCI. Also shown are the resulting subdomains for an exemplary parallel partitioning on 7 processors.

In Fig. 6, the longitudinal wake potential for Variant 1 of the taper geometry is shown. The MAFIA result corresponds to a step size of $\Delta z = 0.1\text{mm}$, $\Delta x = 1\text{mm}$ and $\Delta y = 0.5\text{mm}$. Due to computer memory limitations it was not possible to use a finer mesh in MAFIA. It can be seen that MAFIA does not give sufficiently accurate results for this smoothly tapered structure although the step sizes in all directions are much smaller than the bunch length. A convergent result was obtained in PBCI using a discretization with $\Delta x = \Delta y = \Delta z = 0.25\text{mm}$. PBCI converges to a wake potential which is about 30% lower than the MAFIA result. The loss and kick parameters obtained with the two codes are summarized in Table 2.

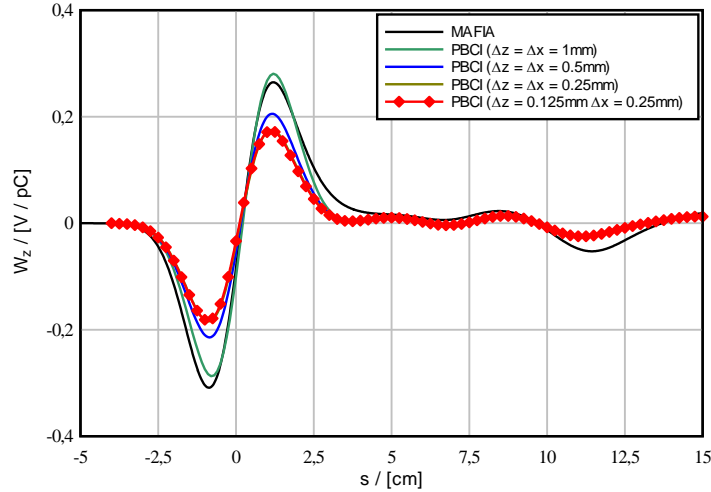


Figure 6: Longitudinal wake potential for Variant 1 of the tapered transition. The curves obtained for different mesh resolutions are shown.

Table 2: Comparison of the loss and kick parameters of the tapered transition obtained with MAFIA and PBCI.

Code	$k_{\parallel} /$ (V/nC)	$k_{\parallel}(1) /$ (V/pC m)	$k_{\perp} /$ (V/pC)
Variant 1 / MAFIA	-7.4	-6.8	138.6
Variant 1 / PBCI	-7.1	-4.8	75.6
Variant 2 / PBCI	-5.2	-4.6	62.8

4.2.3.2 Analysis of the PITZ Diagnostics Section

In this application, the wake fields induced by the different components within the diagnostics double cross of the PITZ injector [22] are estimated. This section is the first in the X-FEL beam line which breaks axial symmetry. Thus, a 3D simulation of the structure is necessary. The geometrical layout of the ten-port vacuum device is shown in Fig. 7. The investigation includes three separate simulations for comparing the influence of the wake fields induced by the different geometrical obstacles within the structure. In the first simulation, the geometry was simplified to the beam tube including only the small step at the entrance of the section. The second simulation included the vacuum vessel without shielding tube. The third simulation considered the full geometry as shown in Fig. 7.

The simulation results for an electron bunch of rms-length 2.5mm are summarized in Fig. 8. For resolving the small details of the geometry, a total of 250 million grid points were needed in the discretization. It was found, in particular, that the small step of 1mm height is responsible for 10-15% of the induced wake fields. The effect of the vacuum vessel inside the cross is about six times higher. The wake field effects are reduced, as expected, when the tube shielding is included.

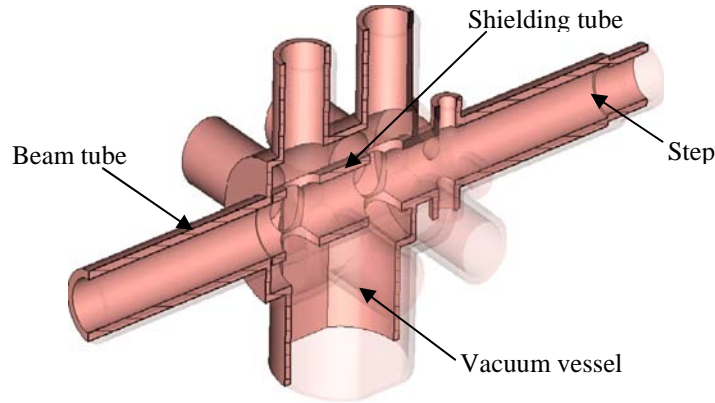


Figure 7: Geometrical view of the diagnostics double cross in the PITZ injector.

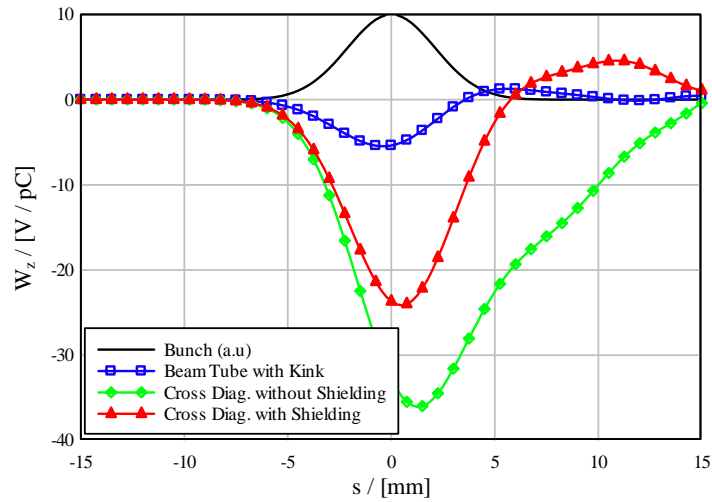


Figure 8: Longitudinal wake potentials induced by the different obstacles within the PITZ diagnostics section.

4.2.3.3 ILC-ESA Collimators

The collimator considered is part of the ILC-ESA test beam program [27]. A schematic view and the dimensions of the structure are shown in Fig. 9. Due to the extremely short bunch length ($\sigma = 300\mu\text{m}$) a discretization with $\Delta x = \Delta y = \Delta z = 20\mu\text{m}$ is used. This results in a computational model with $\sim 4.5 \cdot 10^8$ grid points.

Figure 10 shows the convergence behavior of the longitudinal wake potential with grid resolution. It is interesting to note that convergence is obtained for 10-15 grid points / sigma. This figure corresponds to the standard resolution imposed by wave length in typical FIT simulations. Thus, in this case, the simple stair-step geometry approximation used in the current implementation of PBCI does not seem to influence simulation accuracy.

Figure 11 shows the directly computed part of the wake potential vs. the wake potential transition in the outgoing pipe. The catch-up distance of the wake fields behind the collimator can be estimated to 2.4m. Due to this large distance, the transition potential is expected to dominate the solution. This is clearly seen in Fig. 11.

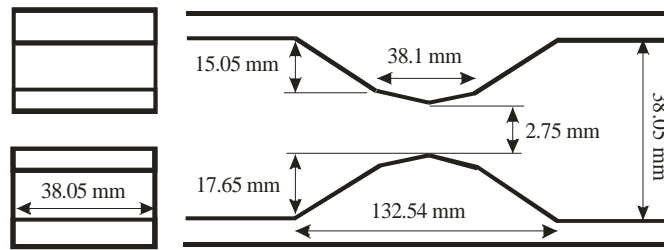


Figure 9: Beam and side views of the collimator #8 for the ILC-ESA test beam experiments.

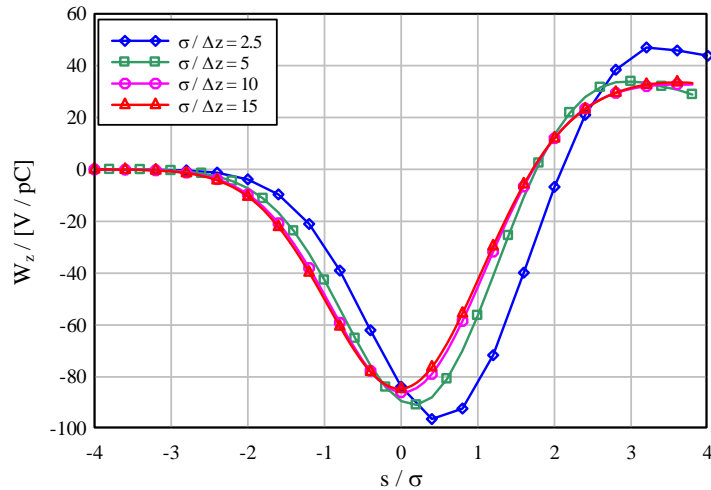


Figure 10: Convergence of the wake potential vs. grid resolution for the ILC collimator #8.

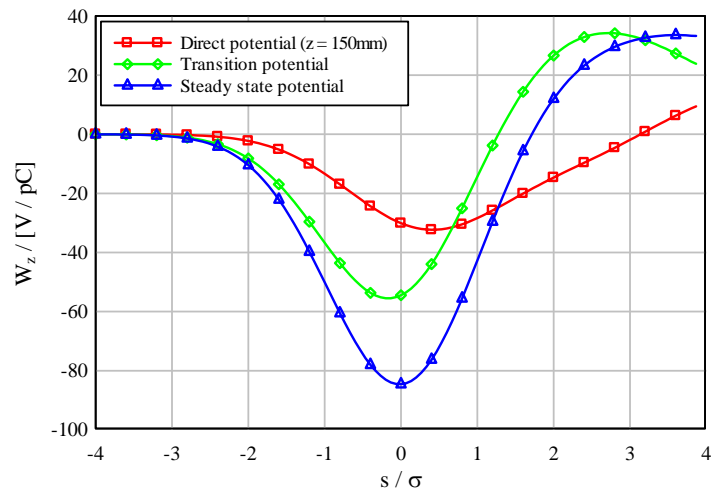


Figure 11: Direct vs. transition wake potential. 150 waveguide modes were used in the computation of the transition wake potential.

4.2.3.4 TESLA HOM-Couplers

Both, the X-FEL and the ILC use accelerating cavities, based on the TESLA superconducting technology. The $\sim 1\text{m}$ long cavities consist of 9 resonating cells which support an accelerating mode at 1.3GHz. At each side of the TESLA cavities two Higher Order Mode (HOM) couplers are mounted on the upstream and downstream beam pipes, respectively. HOM couplers are designed primarily for absorbing the

higher order modes which are excited by the bunch within the cavity. Figure 12 shows the beam view of the X-FEL HOM couplers which will be installed at DESY. Each of them contains a notch filter which reduces the coupling to the accelerating mode. Furthermore, they are rotated with respect to each other by 115° in order to maximize the total coupling to the dipole modes [28].

Figure 13 and 14 show the PBCI results for the transverse wake fields induced by a 1mm bunch passing through the upstream coupler. The curves are shown for different grid resolutions in order to demonstrate the convergence behavior of the solution. In the simulations, a computational window of dimensions $100 \times 100 \times 10 \text{ mm}$ was used. Thus, a moderate discretization with 10 grid points / sigma in each direction already leads to a computational mesh with 10^8 grid points. This figure illustrates the need for parallelization in wake field simulations with short electron bunches. In the present case, a computer cluster with 384 processor cores was used. The computation time on this platform amounts to ~ 12 hours for the largest mesh used (20 points / sigma).

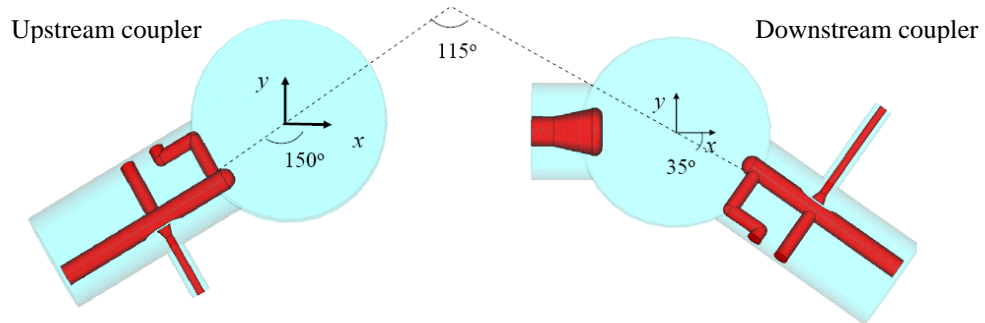


Figure 12: Beam view of the X-FEL upstream and downstream HOM couplers.

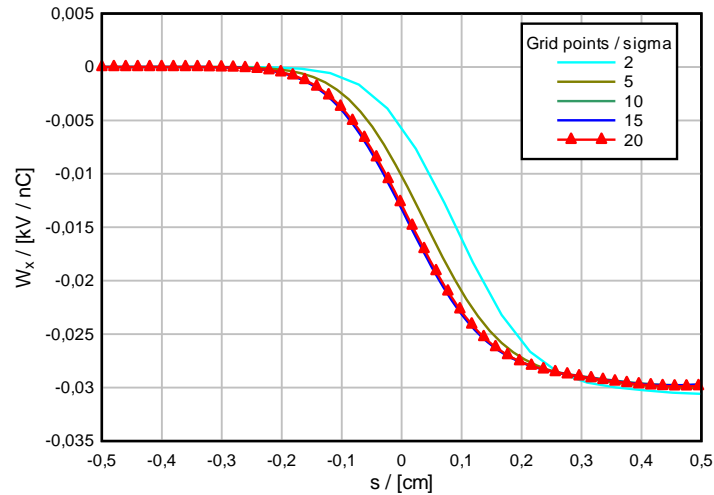


Figure 13: Convergence of W_x vs. grid resolution for the X-FEL upstream coupler.

As in the case of the ICL collimator #8 (Section 4.2.3.3), numerical convergence is obtained for a mesh resolution with 10-15 grid points / sigma. This behavior is typical for difference schemes such as FIT. It indicates that, for short bunches, the mesh size condition imposed by the dominant wave length tends to be more restrictive than the one related to the geometry approximation. This is an important observation knowing the high computational costs which are required by the meshing procedure in the boundary conformal approximation [15].

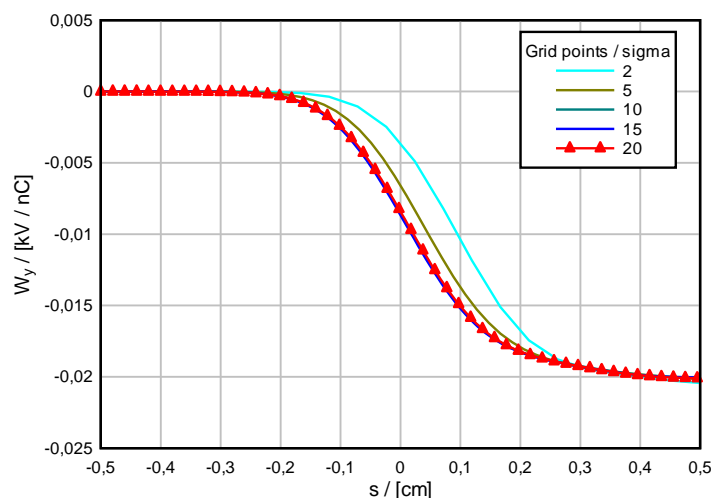


Figure 14: Convergence of W_y vs. grid resolution for the X-FEL upstream coupler.

4.2.4 References

1. A. Chao, B. Richter, C.Y. Yao, "Beam emittance growth caused by transverse deflecting fields in a linear accelerator", Nucl. Instr. Meth., 178 (1980), p. 1.
2. M. Dohlus, R. Lorentz, T. Kemps, H. Schlarb, R. Wanzenberg, "Estimation of the longitudinal wakefield effects in the TESLA-TTF FEL undulator beam pipe and diagnostic section", TESLA-FEL 98-02 (1998).
3. A. Chao, "Physics of Collective Beam Instabilities in High Energy Accelerators", John Wiley & Sons, New York, USA. (1993).
4. T. Weiland, R. Wanzenberg, "Wakefields and Impedances", Proc. of the CAT-CERN Accelerator School (1993), p. 140.
5. K. Balewski, R. Wanzenberg, "Beam Current Limitations in the Synchrotron Light Source PETRA III", Proc. of EPAC'04, Lucerne (2004), p. 2308.
6. PETRA III: A low Emittance Synchrotron Radiation Source, Technical Design Report, DESY 2004-035 (2004).
7. International Linear Collider - Reference Design Report, ILC-REPORT-2007-001 (2007).
8. The European X-Ray Free-Electron Laser - Technical Report, DESY 2006-097 (2006).
9. K. Bane, T. Weiland, "Wake Force Computation in the Time Domain for Long Structures", Proc. of 12th Int. Conf. on High Energy Accelerators, Chicago, IL, USA (1983), p. 314.
10. T. Weiland, "Comment on wake field computation in time domain", Nucl. Instrum. Methods 216, 31 (1983).
11. O. Napoly, Y.H. Chin, B. Zotter, "A Generalized Method for Calculating Wake Potentials", NIM-A, Vol. 334 (1993), p. 255.
12. A. Henke, W. Bruns, "Calculation of Wake Potentials in General 3D Structures", Proc. of EPAC'06, Edinburgh, UK (2006), WEPCH110.
13. I. Zagorodnov, "Indirect Methods for Wake Potential Integration", Phys. Rev. ST Accel. Beams 9, (2006).
14. I. Zagorodnov, T. Weiland, "TE/TM Scheme for Computation of Electromagnetic Fields in Accelerators", J. Comp. Phys., Vol. 207 (2005), p. 69.
15. I. Zagorodnov, R. Schuhmann, T. Weiland, "A uniformly stable conformal FDTD-method in cartesian grids", Int. J. Numer. Model. 16 (2003), p. 127.
16. C. Ng et al, "State of the Art in EM Field Computation", SLAC-PUB-12020 (2006).

17. M. Min, Y.-C. Chae, P.F. Fisher, "Spectral-Element Discontinuous Galerkin Simulations for Wake Potential Calculations: NEKCEM", Proc. of PAC'07, Albuquerque, NM, USA (2007).
18. T. Weiland, "A Discretization Method for the Solution of Maxwell's Equations for Six-Component Fields", Int. J. Elect. Comm., Vol. 31 (1977), p. 116.
19. T. Lau, E. Gjonaj and T. Weiland, "Time Integration Methods for Particle Beam Simulations with the Finite Integration Technique", FREQUENZ, Vol. 59 (2005), p. 210.
20. G. Strang, "On the Construction and Comparison of Difference Schemes", SIAM J. Num. Anal., 5 (1968), p. 506.
21. G. Aharonian, R. Meller, R.H. Siemann, "Transverse wake field calculations", CLNS Report, CLNS 82/535 (1982).
22. A. Oppelt et al, "Status and first results from the upgraded PITZ facility", Proc. of FEL'05, Stanford, CA (2005), p. 564.
23. F. Wolfheimer, E. Gjonaj, T. Weiland, "A Parallel 3D Particle-In-Cell (PIC) with Dynamic Load Balancing", Nucl. Inst. Meth. in Phys. Res. A, Vol. 558 (2006), p. 202
24. K. Balewski, R. Wanzenberg, "The Impedance of Selected Components of the Synchrotron Light Source PETRA III", Proc. of PAC'05, Knoxville, (2005), p. 1752.
25. R. Wanzenberg, K. Balewski, E. Gjonaj, "Wake Computations for Undulator Vacuum Chambers of PETRA III", Proc. of PAC'07, Albuquerque, NM, USA (2007), FRPMN01.
26. MAFIA Version 4.106, CST GmbH, BÜdingerstr. 2a, D-64289 Darmstadt, Germany (2002).
27. N. Watson et al, "Direct Measurement of Geometric and Resistive Wakefields in Tapered Collimators for the International Linear Collider", Proc. of EPAC'06, Edinburgh, UK (2006), MOPLS06.
28. I. Zagorodnov, M. Dohlus, "Coupler Kicks", Proc. of ILC'07, Hamburg, Germany (2007).
29. K. Balewski, R. Wanzenberg, O. Zagorodnova, "The Impedance Model of PETRA III", this ICFA Beam Dynamics Newsletter.

4.3 Wakefields and Impedances at Elettra and FERMI@Elettra

E. Karantzoulis, C. Bontoiu, P. Craievich
 Sincrotrone Trieste S.C.p.A.
 Strada Statale 14 - km 163,5 in AREA Science Park
 34012 Basovizza, Trieste ITALY
 Mail to: Emanuel.karantzoulis@elettra.trieste.it

4.3.1 Introduction

Understanding wake fields and impedances is of great importance for the performance of accelerators. Instabilities driven by the wakes of the beams can very much limit the performance of accelerators in both beam intensity and quality. At Elettra there has always been a strong activity concerning wake fields, including also many measurements and observation on the storage ring like the impedance evolution with the addition of many low vertical gap vacuum chambers or the impedance increase due NEG coated chambers [6]. With the advent of the modern free-electron lasers in the last decade, the wakefield/impedance problem has significantly grown up since the beam quality may be seriously degraded, limiting thus the lasing process itself or even worse,